Journal of Materials Chemistry C

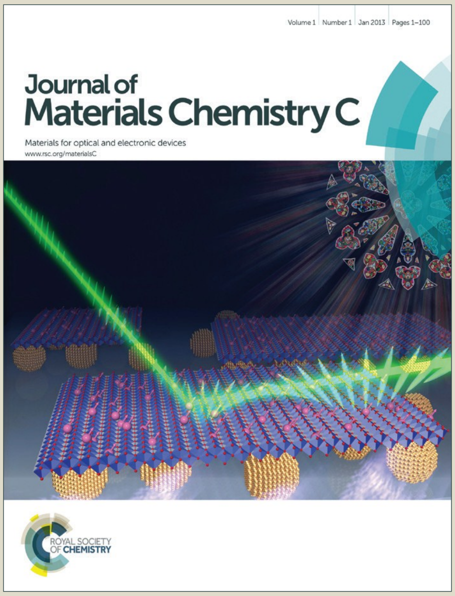

Volume 1 | Number 1 | Jan 2013 | Pages 1–100

Journal of Materials Chemistry C

Materials for optical and electronic devices

www.rsc.org/materialsC

ROYAL SOCIETY OF CHEMISTRY

ROYAL SOCIETY OF CHEMISTRY

www.rsc.org/materialsC

Journal Name

ARTICLE

Vertical SnO_2 Nanosheets@SiC Nanofibers with Hierarchical Architecture for High-Performance Gas Sensors

Received 00th January 20xx,
Accepted 00th January 20xx

DOI: 10.1039/x0xx00000x

www.rsc.org/

Bing Wang,[a] Yingde Wang,*[a] Yongpeng Lei,*[b] Song Xie,[a] Nan Wu,[a] Yanzi Gou,[a] Cheng Han,[a] Qi Shi[a] and Dong Fang[c]

Increasing demands for detection of harmful gases in harsh environments have stimulated considerable efforts to develop novel gas sensor with high sensitivity, superior thermal/chemical stability and fast response/recovery rate. In this paper, we report the vertical growth of ultrathin SnO_2 nanosheets (SnO_2 NSs) on quasi-one-dimensional SiC nanofibers (SiC NFs) forming a hierarchical architecture via a simple hydrothermal method. In comparison to pure SnO_2 NSs, the SnO_2 NSs@SiC NFs hierarchical composite shows an ultrafast response/recovery rate, high sensitivity, and simultaneously excellent reproducibility to various target gases including ethanol, methanol, hydrogen, isopropanol, acetone and xylene, even at high temperature. The response times are less than 5 s with corresponding recovery times < 15 s. Furthermore, the SnO_2 NSs@SiC NFs gas sensor shows a superior sensing selectivity and long-term stability to ethanol. The hierarchical architecture and synergetic effect of the SnO_2-SiC heterojunction as well as plenty of active sites from the vertically ultrathin SnO_2 NSs play critical roles for the superior sensing performance of SnO_2 NSs@SiC NFs. This work highlights the possibility to develop novel high-performance gas sensor for application in harsh environments.

Introduction

In situ detection of gases hazardous to the environment and human health has attracted increasing attention.[1,2] In the past decades, metal-oxide semiconductor based gas sensors have been extensively investigated for various daily and industrial applications due to their outstanding sensing performance, even in harsh environments.[1,3,4] Thereinto, *n*-type tin dioxide (SnO_2) has been proved to be promising for gas sensing by virtue of its excellent photoelectrical properties, superior thermal stability (melt point is 1127 °C), chemical inertness, low cost and nontoxicity.[5,6] The sensing mechanism of SnO_2 gas sensors is based on the electrical conductivity change of the sensor in different types of target gases.[7] In general, when SnO_2 is exposed in air, the electron from its conduction band (CB) will transfer to the absorbed oxygen, resulting in production of tremendous oxygen species (O^{2-}, O^- or O_2^-) on the SnO_2 surface. Simultaneously, an electron-depleted surface layer forms on SnO_2, which leads to a decrease in the electrical conductivity. In reducing gases (e.g., ethanol, hydrogen, and methanol), the target gases will react with those oxygen species, freeing electron back to the SnO_2 surface, leading to an increase in the sensor conductivity.[8] In oxidizing gases (electron acceptor), more electrons are grabbed by the absorbed gases, further lower the electrical conductivity of the sensor. Recently, SnO_2 with different nanostructures (nanosheets, nanoparticles, nanowires, nanospheres, nanotubes, etc.) have been reported for detecting various types of gases.[8] Moreover, to reach higher sensitivity, strategies such as doping with noble metals,[9,10] forming heterojunction with other semiconductors[11,12] and exposing active facets[13] have been demonstrated.

Besides sensitivity and durability, the response/recovery behavior is also a vital characteristic parameter for gas sensors. With a fast response/recovery rate, large loss/harm can be averted in time. However, achieving of rapid response and recovery characteristics for these nanostructured gas sensors is still a challenge.[14] To promote the response/recovery speed, a promising way is to construct hierarchical architectures, which can simultaneously avoid the agglomeration of SnO_2 nanostructures and facilitate the diffusion (adsorption and desorption) of target gas.[15] For instance, Lee *et al.* have demonstrated that the core-shell ZnO-SnO_2@carbon nanofibers exhibited excellent sensing performance including fast response/recovery properties, high sensitivity and ultralow detection limit.[16] The polypyrrole/SnO_2 hybrid also showed very fast response and high sensitivity to ammonia gas.[17] Three-dimensional mesoporous graphene aerogel has been utilized to support SnO_2 nanocrystals for high performance NO_2 gas sensor.[18] However, most of the reported substrates including carbonaceous materials (graphene, carbon nanotubes, carbon nanofibers, etc.) and organic substrates (poly(ethylene

---

[a] *Science and Technology on Advanced Ceramic Fibres and Composites Laboratory, National University of Defense Technology, 109 Deya Road, Changsha 410073, PR China.* E-mail: wyd502@163.com.*

[b] *College of Basic Education, National University of Defense Technology, Changsha 410073, PR China;* E-mail: lypkd@163.com.*

[c] *College of Materials Science and Engineering, Wuhan Textile University, Wuhan 430074, PR China.*

Electronic Supplementary Information (ESI) available: supplemental Figures and table. See DOI: 10.1039/x0xx00000x terephthalate), polypyrrole and polyimide) cannot meet the requirements to apply in certain fields like ethanol direct solid oxide fuel cells (EDSOFCs), power generation, aerospace, automotive, avionics, industrial process control, nuclear power and well-logging industries due to the harsh work environments (e.g., high temperatures, corrosive environments, and high frequency).[19-23] For instance, ethanol gas sensors have been widely applied in breath analyzers for drivers, detecting ethanol in foodstuffs experiments to assess the development of bacteria and fungi in food and monitoring the chemical processes in chemical industries.[24] However, most of the reported works were focus on the low/room temperature ethanol gas sensors because they are more desired for application in the fields mentioned above. But these ethanol sensors cannot satisfy the requirements to monitor the ethanol leakage and/or its total combustion process in the EDSOFCs, whose operating temperature is typically in the range of 500~1000 °C.[22,23] Hence, it is more desired but challenging to develop novel gas sensor capable of withstanding aforementioned harsh environments.

As a wide band gap semiconductor, silicon carbide (SiC) has emerged as an ideal candidate for application in harsh environments.[25] More recently, SiC based gas sensors have attracted an increasing attention due to its chemical inertness, excellent thermal stability, high thermal conductivity, high electron mobility, compatibility with conventional Si-based integrated devices.[26,27] The high electron mobility of SiC is beneficial to quickly shuttle the charge carriers, which offers an opportunity to design SiC based gas sensor with ultrafast response/recovery rate. Therefore, combining SiC with highly reactive SnO_2 is expected to develop novel high performance gas sensor capable of applying in harsh environments. Furthermore, it has been demonstrated that the composite of SnO_2 nanobelts@SiC foams showed efficient performance to detect low concentration of NH_3 and NO_2.[28] Whereas the response/recovery speed was very slow.

In the present paper, ultrathin SnO_2 nanosheets (SnO_2 NSs) were in situ grown on the quasi-one-dimensional SiC nanofibers (SiC NFs) forming a hierarchical SnO_2 NSs@ SiC NFs composite via a simple hydrothermal method. The synthesized SnO_2 NSs@SiC NFs sample shows a high sensitivity, excellent reproducibility, outstanding selectivity, long-term stability and particularly ultrafast response/recovery speed toward ethanol. Such a superior sensing performance is attributed to the synergetic effect of SnO_2 and SiC and the hierarchical architectures as well as the plenty of active sites from the vertically ultrathin nanosheets with large surface to volume ratios. This work demonstrates a simple strategy to design high performance gas sensor which can be applied in harsh environments.

Experimental Section

Materials

Polyacrylonitrile (PAN, M_n = 120 000 g mol^{-1}, Kaneka, Japan), Si powders (200 mesh, Sinopharm, China), tin dichloride dihydrate ($SnCl_2{\cdot}2H_2O$, Sigma-Aldrich Co., UK), mercaptoacetic acid (MA, Sigma-Aldrich Co., UK), N,N-dimethylformamide (DMF, Hengxing, China), NaOH (Sigma-Aldrich Co., UK) and HCl (37 wt%, Hengxing, China) were all analytical reagents and used as-received without any further purification.

Fabrication of mesoporous SiC NFs

Typically, 1.2 g PAN powders were dissolved in 10 ml DMF under vigorous stirring at 30 °C for 5 h to prepare the spinning solution. And then the homogeneous spinning solution was loaded into a 10 ml volume plastic syringe with a needle of 0.8 mm inner diameter. Electrospinning was carried out with a power supply (Dongwen, China) of 18 kV applied on the needle and aluminum foil film collector with a distance of 25 cm. The feedrate was kept at 0.9 ml h^{-1} with a syringe pump (Longer Pump LSP02-1B, China). After curing the as-received PAN nanofibers at 260 °C for 1 h in flowing air (1 °C min^{-1}), the obtained nanofibers were carbonized at 1000 °C for 1 h (2 °C min^{-1}) to obtain CNFs. To synthesize SiC NFs, excessive Si powders were placed at the bottom of the alumina crucible and the as-received CNFs were laid on the top of the silicon powders with a distance of 1.5 cm. Then the alumina crucible was heated to 1500 °C for 5 h (10 °C min^{-1}) in a horizontal furnace (Tianjin Zhonghuan, China) under Ar atmosphere.

Alkali treatment of the SiC NFs

Prior to hydrothermal reaction, the resultant SiC NFs were treated with alkali solution. In detail, 25 mg SiC NFs were immersed in 20 ml NaOH solution (5 M) for 12 h at room temperature. Afterward, the treated SiC NFs were washed with deionized water for 5 times and dried at 80 °C for 12 h.

Fabrication of the hierarchical SnO_2 NSs@SiC NFs

SnO_2 NSs were in situ grown on the alkali-treated SiC NFs by a simple hydrothermal method. Typically, 0.1 g $SnCl_2{\cdot}2H_2O$ was dissolved in 30 ml MA solution (10 mM), followed by adding 0.5 g urea and 0.5 ml HCl solution. The mixture solution was stirred for 2 min in air at 25 °C and then was transferred into the Teflon-lined stainless-steel autoclave. Subsequently, 10 mg of the basic-treated SiC NFs were immersed into the above solution. The autoclave were sealed up and heated to the target temperature (100-180 °C) in an electric oven and maintained for 6 h. After naturally cooling to the room temperature, the resultant sample was washed with a mixture solvent of ethanol and water (v/v = 1:1) for several times and dried at 80 °C for 12 h. Finally, the samples were calcined at 600 °C for 2 h with a heating rate of 5 °C min^{-1}.

Characterization

The morphological features of the catalysts were analyzed by using Hitachi S-4800 field-emission scanning electron microscope (FE-SEM) with an acceleration voltage of 5.0 kV and JEM-2100 high resolution transmission electron microscope (HRTEM). X-ray diffraction (XRD) data were collected from 10 to 80° (2θ) on Bruker AXS D8 Advance device using Cu-$K\alpha$ radiation (λ = 1.5418 Å) at a scanning rate of 2θ = 0.02° per step. X-ray photoelectron spectroscopy (XPS) was conducted on a Thermo Scientific ESCALAB 250Xi machine with an Al Kα source. And the spectra were quantified and analyzed using XPSPEAK 4.1 software. The thermal stability of the SnO_2 NSs@SiC NFs was evaluated at the temperature range from 30 to 800 °C by using a thermogravimetric analyzer (Pyris 1 TGA, PerkinElmer) with heating rateof 10 °C min^{-1} in air. The Brunauer-Emmett-Teller (BET) surface areas (S_{BET}) of samples were estimated from nitrogen adsorption isotherm (BELSORP-mini II, Japan). The pore size distributions were determined using the Barrett-Joyner-Halenda (BJH) method.

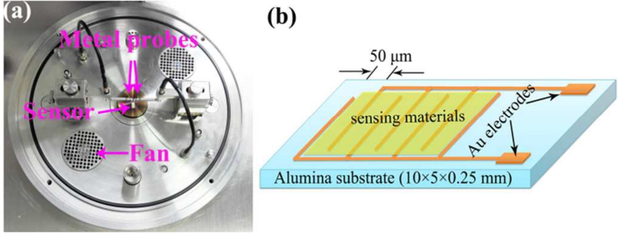

Fig. 1 (a) Photograph of the gas sensing testing equipment CGS-1TP and (b) schematic illustration of the gas sensor device.

Gas sensing measurements

The gas sensing performances of the samples were measured in an intelligent gas sensor analysis system (CGS-1TP, Beijing Elite Tech Co., Ltd., China) as shown in Fig. 1a, which was commonly used to test the gas sensing behaviors.[18] The operating temperature can be modulated from room temperature to 500 °C with a heating rate of 5 °C s^{-1}. First, the prepared sensing materials were mixed with deionized water (10 mg ml^{-1}) to form a homogeneous paste. Gas sensing devices were fabricated by coating the pastes (20 μl) on commercial aluminum substrates (10 mm×5 mm×0.25 mm) with Au interdigitated electrodes (AURORA technologies, China) as illustrated in Fig. 1b. Subsequently, the prepared sensors were naturally dried in air for several hours. During the sensing measurement, the Au electrodes were pressed under the metal probes to achieve electrical contact (Fig. 1a). After the sensor was heated to the target temperature and the resistance kept at almost a constant level, the calculated amount of target gases (chromatographic pure) were injected into the test chamber (18 L in volume). At the same time, the fans were turned on to ensure a uniform concentration of the target gases in the chamber. Finally, the test chamber was opened to make the sensor exposing in air that the resistance of the sensor was recovered. The sensor response (sensitivity) is defined as S = Rg/Ra in reducing gases for n-type semiconductor, where Ra and Rg are the resistance of the sensor in air and in the target gas, respectively. The response/recovery time was defined as the time needed to reach 90% of the saturation resistance change after introducing target gas or exposing in air.

Results and Discussion

The SnO_2 NSs@SiC NFs hybrids were synthesized by growing vertical SnO_2 NSs on the SiC NFs via a simple hydrothermal method as illustrated in Scheme 1. Prior to hydrothermal reaction, the as-received SiC NFs were treated in 5 M NaOH solution to introduce hydroxyl (-OH) group as well as to remove the silica on the surface of SiC NFs. After immersing SiC NFs into the mixed solution of $SnCl_2$, urea and MA, Sn^{2+} with positive charge was easily absorbed on the OH-terminated SiC NFs (negative charge) due to the electrostatic interactions. During the hydrothermal reaction, tin oxides (SnO_x) firstly nucleated on the SiC NFs followed by Ostwald ripening process to form nanosheet morphology. Urea in the solution can promote the nucleation of Sn^{2+} to form nanocrystals while MA plays a critical role in the formation of nanosheets.[18,29] Moreover, the higher hydrothermal reaction temperature leads to the fast nucleation and growth of SnO_2 crystals, thus forming rod-shaped SnO_x on the SiC NFs. In addition, the abundance of -OH groups and MA additive can not only ensure the formation of NSs, but also enable the SnO_2 NSs to connect with SiC NFs

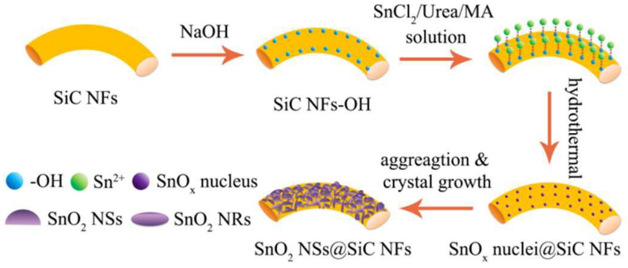

Scheme 1 Schematic illustration of the synthesis process for SnO_2 NSs@SiC NFs.

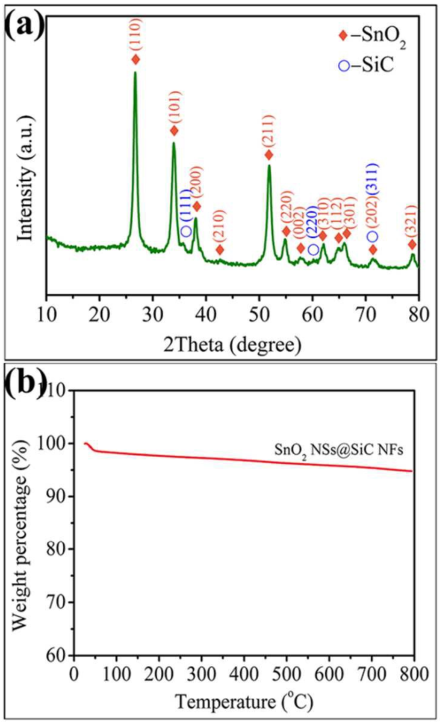

Fig. 2 (a) XRD pattern and (b) TGA analysis of the SnO2 NSs@SiC NFs hierarchical composite.

tightly, which will minimize the boundary and promote the electron transfer between the SnO_2 NSs and SiC NFs. The zeta potential of SnO_2 NSs@SiC NFs is measured to be -11.1 mV, implying that the SnO_2 NSs@SiC NFs is highly of negatively charged (Fig. S1, ESI†).

Fig. 2 is the XRD pattern and TGA analysis of the resultant SnO_2 NSs@SiC NFs hierarchical composite. It is clear that the hierarchical composite is composed of two mixed phases of tetragonal rutile SnO_2 (JCPDS card no. 41-1445) and cubic SiC (JCPDS card no. 29-1129) (Fig. 2a).[27,30] The sharp peaks and the absence of other impurities imply a high crystallinity and purity of the hierarchical composite. The average crystallite size of the SnO_2 NSs is calculated to be 10 nm by using Scherrer formula: $d = 0.9\lambda/B\cos\theta$, where B is the width of the diffraction peak at half its maximum intensity, λ is the X-ray wavelength, and θ is the maximum diffraction angle. To investigate the stability of the SnO_2 NSs@SiC NFs sample, TGA test was conducted from room temperature to 800 °C in air. As shown in Fig. 2b, the weight loss happened below 100 °C is ascribed to the evaporation of water and other absorbed species. There is no dramatically weight change along with the increasing temperature to 800 °C, suggesting the excellent stability and great potential of the sample for high temperature application.

The morphologies and microstructures of the SiC NFs and SnO_2 NSs@SiC NFs hybrid were characterized by SEM (Fig. 3). For SiC NFs, a rough fiber surface is observed (Fig. 3a), which is beneficial for the nucleation of SnO_x. According to the general SEM image (Fig. 3b), SnO_2 NSs are uniformly grown on all of the SiC NFs without existing in the gap of the fibers at the reaction temperature of 120 °C. The diameter of the SnO_2 NSs@SiC NFs hybrid is about 400 nm in comparing to 200 nm of the pure SiC NFs, implying that the vertical SnO_2 NSs is about 100 nm in height. As shown in Fig. 3c, it is obvious that the well-defined ultrathin SnO_2 NSs are interconnected with each other, supplying a multipath electron transfer channel, which may be propitious to accelerate the response rate. The thicknesses of the interconnected SnO_2 NSs are calculated to be less than 5 nm (inset in Fig. 3c). At a low reaction temperature of 100 °C, no SnO_2 NSs but nanoparticles are generated on the SiC NFs (Fig. S2a, ESI†). While SnO_2 nanorods (SnO_2 NRs) are observed on the SiC NFs when the temperature rises up to 160 °C (Fig. S2b, ESI†). From the viewpoint of architecture, more SnO_2 located on the surface of ultrathin SnO_2 NSs can react with the target gas due to the high surface to volume ratio of nanosheets. In the case of SnO_2 NRs, the SnO_2 in the internal of the nanorods cannot contact with the target gas, leading to the relatively lower availability of the SnO_2 NSs. It is also demonstrated that there are four elements Si, C, O and Sn in the SnO_2 NSs@SiC NFs composite from the EDS spectrum (Fig. 3d). The Au element is from the sputtered Au particles for SEM measurement.

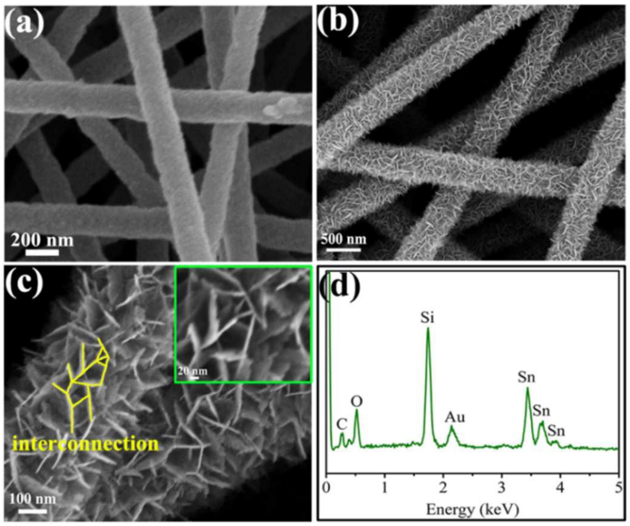

Fig. 3 SEM images of (a) SiC NFs and (b) the SnO_2 NSs@SiC NFs hierarchical hybrids synthesized at the reaction temperatures of 120 °C at low magnification; (c) at high magnification; (d) EDS spectrum of the SnO_2 NSs@SiC NFs hybrid. The inset in (c) is the close view of the interconnected NSs with thickness less than 5 nm.

Fig. 4 shows the TEM images of SiC NFs and SnO_2 NSs@SiC NFs hierarchical composite. SiC NFs with a diameter of about 200 nm and rough surface are clearly illustrated in Fig. 4a. The HRTEM image in Fig. 4b reveals the lattice spacing of 0.251 nm assigned to (111) plane of SiC. For SnO_2 NSs@SiC NFs, the overall TEM image (Fig. 4c) indicates that SiC NFs are uniformly covered by SnO_2 NSs with thickness of several nanometers. The composite fiber is of 400 nm in diameter, which is in agreement with the SEM result (Fig.

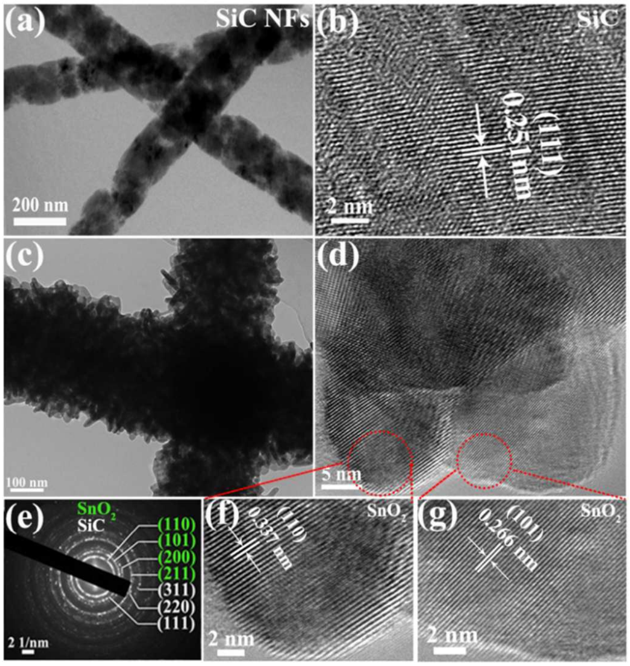

Fig. 4 (a) TEM images of (a) SiC NFs and (c) SnO_2 NSs@SiC NFs at low magnification; (b) and (d) corresponding HRTEM images

of SiC NFs and SnO_2 NSs@SiC NFs, respectively; (e) SAED of SnO_2 NSs@SiC NFs; (f) and (g) magnified HRTEM image of the SnO_2 NSs.

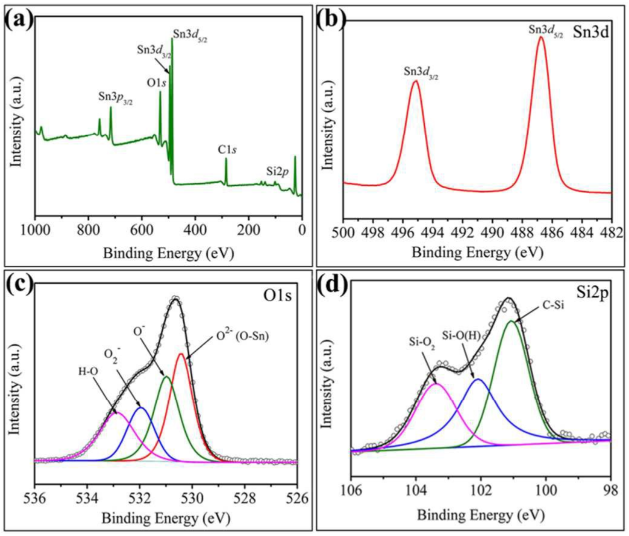

Fig. 5 XPS analysis of SnO_2 NSs@SiC NFs: (a) survey spectrum; (b) Sn3d; (c) O1s and (d) Si2p.

3b). The selected area electron diffraction (SAED, Fig. 4e) pattern of the SnO_2 NSs@SiC NFs hybrids with well-defined rings is composed of two parts. The rings from inside to outside with corresponding planes marked with blue colour are indexed to (110), (101), (200) and (211) planes of rutile SnO_2, while the rings from inside to outside with corresponding planes marked with white colour are indexed to (111), (220) and (311) planes of cubic SiC. As shown in the HRTEM image (Fig. 4d), the fan-shaped SnO_2 NSs with tens of nanometers in width are clearly observed. It has also demonstrated the fringe spacing of 0.337 and 0.266 nm (Fig. 4f and g), which are consistent with the (110) and (101) planes of SnO_2 NSs.[12,31] These results further confirm the hierarchical structure of SnO_2 NSs@SiC NFs, which is composed of rutile SnO_2 and cubic SiC as depicted in the XRD pattern (Fig. 2a). To further investigate the chemical composition and bonding states, XPS analysis of the SnO_2 NSs@SiC NFs hybrid is carried out. Fig. 5a exhibits the survey scan XPS spectrum of the SnO_2 NSs@SiC NFs, which confirms the presence of four elements including Si, C, Sn and O in the sample. The high resolution Sn 3d spectrum (Fig. 5b) shows two typical peaks at the binding energies of 495.1 and 486.7 eV corresponding to the Sn $3d_{3/2}$ and Sn $3d_{5/2}$ states of Sn^{4+} with spin-orbit splitting of 8.4 eV, indicating the presence of SnO_2.[18,32,33] The deconvolution of the O 1s peak (Fig. 5c) displays four peaks at 530.4, 531.0, 532.0 and 532.9 eV, which belong to O^{2-} and/or O-Sn bond in SnO_2, O^-, O_2^- and -OH, respectively.[4,34] These oxygen species (O^{2-}, O^- and O_2^-) may originate from the adsorption of oxygen on the surface of SnO_2 followed by receiving electron from the CB of SnO_2. As known, large amounts of oxygen species are beneficial for enhancing the sensitivities of gas sensors. The deconvoluted O 1s peaks at higher binding energy may be ascribed to the chemisorbed -OH (from H_2O) on the surface of SnO_2.[35] In the Si 2p high resolution spectrum (Fig. 5d), the peak at the binding energy of 101.0 eV representing Si-C bond is observed, implying the existence of SiC. Additional peaks at 102.1 and 103.4 eV in Fig. 5d are ascribed to the Si-O(H) and Si-O_2 bonds in the SiC NFs,[36] which may be attributed to the surface oxidization of SiC during hydrothermal reaction and/or the attached -OH group on SiC after basic treatment.

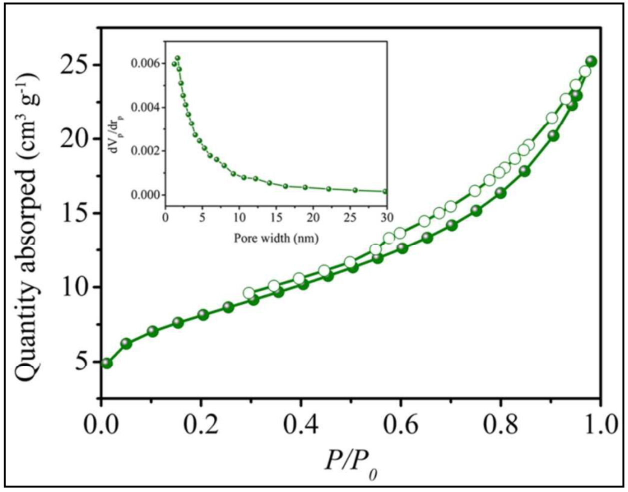

Fig. 6 N_2 adsorption-desorption isotherm of SnO_2 NSs@SiC NFs. The inset is the corresponding pore size distribution.

The specific surface area and pore size distribution of the SnO_2 NSs@SiC NFs hierarchical composite were further characterized by N_2 adsorption-desorption measurements. The isotherm illustrated in Fig. 6 reveals a typical IV adsorption branches with a H3 hysteresis loop according to IUPAC classification,[37] implying there are abundant slit-shaped mesopores resulted from the packed nanosheet-like SnO_2 on the the SiC NFs. The BET surface area of SnO_2 NSs@SiC NFs is calculated to be 28.6 m^2 g^{-1} with total pore volume of 0.04 cm^3 g^{-1}. The pore size distribution determined by the BJH method is calculated to be in the range of 0.2-15 nm. While the BET surface area of pure SnO_2 NSs is 14.1 m^2 g^{-1} with total pore volume of 0.016 cm^3 g^{-1} (Fig. S3, ESI†). The results indicate the hierarchical SnO_2 NSs@SiC NFs have a higher sensing area than the pure SnO_2 NSs. The low surface area may be attributed to the aggregation of the pure SnO_2 NSs as shown in the SEM image (Fig. S4, ESI†).

The gas sensing performances of the commercial SnO_2 powders, pure SnO_2 NSs and SnO_2 NSs@SiC NFs hierarchical composite were evaluated by their resistance changes upon exposure to target gases with a controlled concentration. It is well known that the response of gas sensor is greatly affected by the operating temperature. To determine the optimum one, all of the gas sensors were tested at the temperature from 200 to 500 °C towards 100 ppm ethanol as the results exhibited in Fig. 7a. It can be seen that the sensitivities of pure SnO_2 NSs and SnO_2 NSs@SiC NFs sensors are higher than that of commercial

SnO_2 powders, indicating the advantages of SnO_2 NSs for gas sensing. However, almost negligible signal was obtained with the presence of 100 ppm ethanol gas for pure SiC NFs sensor from 200 to 500 °C (Fig. S5, ESI†), indicating the poor sensing performance of SiC NFs for ethanol gas detection. Obviously, along with the rising operating temperature, the sensitivities (S=Ra/Rg) of the three sensors increase initially to the highest value and then drop with further increase of the temperature. The optimum temperature is found to be 350 °C for the sensors based on pure SnO_2 NSs and SnO_2 NSs@SiC NFs. At relatively low temperature (<350 °C), the low sensitivity can be attributed to the insufficient energy to overcome the reaction activation energy barrier.[38] At the temperature higher than 350 °C, the reduction in sensitivity may be due to the difficulty in exothermic gas adsorption.[39] It has been demonstrated that the interaction between gas molecules and SnO_2 surface is an exothermic reaction. [40] The accumulation of large amount of heat energy on the SnO_2 surface leads to the fast desorption of gas molecules before reacting with the oxygen species on SnO_2 surface at higher temperature,[34] resulting in an obvious drop in sensor response. The higher sensitivity of SnO_2 NSs@SiC NFs sensor than that of pure SnO_2 NSs sensor is contributed to the heterojunction effect of SnO_2 and SiC, the specific hierarchical structure and the vertical growth of SnO_2 NSs. Excitingly, the SnO_2 NSs@SiC NFs sensor still presents a high sensitivity of 7.2 (*vs.* 3.1 for pure SnO_2 NSs sensor) even at the high temperature of 500 °C, confirming the great potential of SnO_2 NSs@SiC NFs for application in high temperature environments. An additional reason may be attributed to the high thermal conductivity of SiC, which can rapidly remove part of heat energy to keep the redox reaction on the SnO_2 surface.

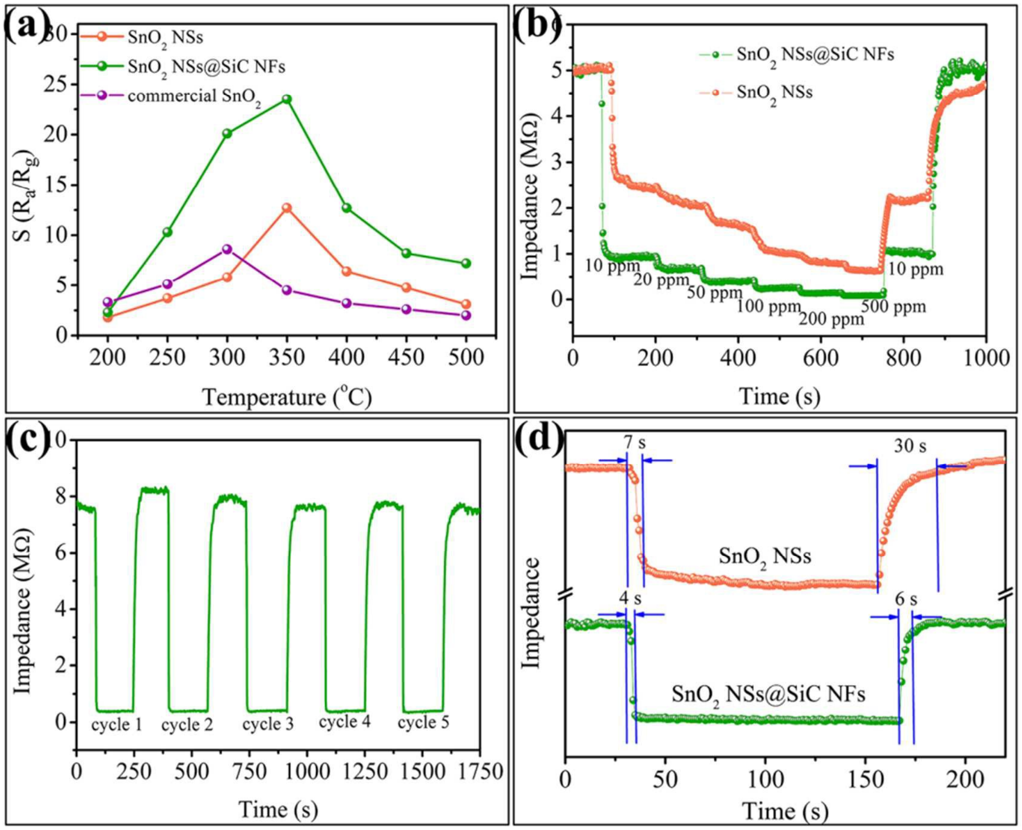

Fig. 7 (a) Sensor responses of the pure SnO_2 NSs and SnO_2 NSs@SiC NFs to 100 ppm ethanol at different operating temperatures; (b) dynamic sensing response of pure SnO_2 NSs and SnO_2 NSs@SiC NFs toward various ethanol concentrations at 350 °C; (c) sensing reproducibility of the SnO_2 NSs@SiC NFs hierarchical composite sensor and (d) comparison of the response time and recovery time between pure SnO_2 NSs and SnO_2 NSs@SiC NFs, ethanol concentration is 100 ppm, operating temperature is 500 °C. Response and recovery time were defined as the time needed to reach 90% of total signal change, respectively.

Fig. 7b shows the dynamic sensing responses of the sensors based on pure SnO_2 NSs and SnO_2 NSs@SiC NFs toward various ethanol concentrations (10-500 ppm) at the optimized temperature of 350 °C. It can be found that the sensitivities of both the sensors are highly dependent on the ethanol concentration in the measurement range. As the sensitivity-concentration plot shown in Fig. S6 (ESI†), the sensitivities of the two sensors almost increase linearly with the increment of ethanol concentration, particularly at the concentration lower than 100 ppm. The successive response change exhibits the consecutive detection capability of the sensors to target gases even at high temperature. Moreover, the resistance of the sensor goes back to almost the same value when 10 ppm ethanol was injected into the chamber again. The result suggests the excellent reproducibility of the SnO_2 NSs@SiC NFs sensor.

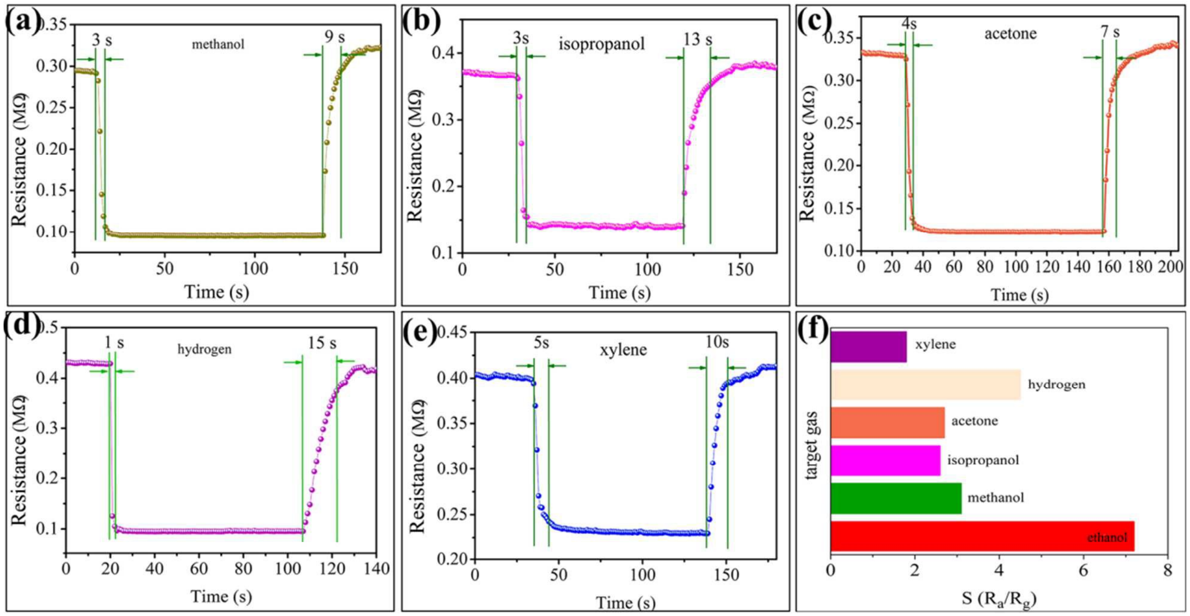

Fig. 8 Ultrafast response/recovery performance of the SnO_2 NSs@SiC NFs hierarchical composite sensor toward: (a) methanol; (b) isopropanol; (c) actone; (d) hydrogen and (e) xylene; (f) is the comparison of the sensitivity among various gases, implying the high selectivity of the sensor toward ethanol. The gas concentration is 100 ppm and the operating temperature is 500 °C.

Similar orderliness between sensitivity and concentration can also be obtained at the elevated temperature of 500 °C (Fig. S7, ESI†), implying the outstanding sensing behavior at high temperature. The sensitivities of SnO_2 NSs@SiC NFs sensor are from 3.9 to 63.2 for 5-500 ppm ethanol, which is higher than that of the pure SnO_2 NSs sensor (1.8-28.4) under the same concentration, further demonstrating the superior sensing performance of SnO_2 NSs@SiC NFs. Even when the ethanol concentration is as low as 500 ppb, the sensitivity of SnO_2 NSs@SiC NFs sensor can reach to 1.2 (Fig. S8, ESI†), indicating the low detect limit of the sensor.

To investigate the reproducibility of the SnO_2 NSs@SiC NFs sensor, the same sensor was exposed to ethanol with the same concentration for 5 cycles (Fig. 7c). Evidently, consistent sensing responses with excellent recovery characteristics were observed in comparing to the usually significant baseline drift for SnO_2 sensor,[1] indicating the excellent reproducibility of our sensor. The response and recovery times (τ_{res} and τ_{recov}), which are accordingly defined as the time to achieve 90% of the total resistance change in the case of adsorption (reaching the maximum response) and desorption (back to the original resistance), are also important characteristic parameters for gas sensors. As shown in Fig. 7d, the τ_{res} and τ_{recov} of SnO_2 NSs@SiC NFs sensor are accordingly to be 4 and 6 s at 500 °C, which are much faster than those of SnO_2 NSs sensor (7 and 30 s, respectively) and commercial SnO_2 powders (11 s and 29 s, respectively. Fig. S9, ESI†). Even at the temperature of 350 °C, the SnO_2 NSs@SiC NFs sensor show a τ_{res} of 6 s and τ_{recov} of 35 s, corresponding to 1.6 and 5 times faster than those of pure SnO_2 NSs sensor (Fig. S10, ESI†). Very recently, the hierarchical Zn doped SnO_2 nanosheets were reported to present a slow τ_{res} of 14 s toward 100 ppm ethanol at 320 °C.[41] Such rapid response and recovery speeds of our sensor are ascribed to the specific hierarchical architectures and the vertically ultrathin nanosheet morphology, which can maximize the contact area between the gas molecules and sensor to facilitate the adsorption and desorption of the ethanol molecular. In the case of pure SnO_2 NSs, it can be seen that the sphere-like SnO_2 NSs obviously aggregates together and some SnO_2 NSs are covered by nanosheets (Fig. S4, ESI†), which results in the low effective reactive area and the resort of the gas.

The advantages of the hierarchical structure to accelerate the adsorption and desorption of target gases were also validated by measuring the response/recovery characteristics of the SnO_2 NSs@SiC NFs sensor towards various gases (e.g., reducing gases methanol, isopropanol, actone, hydrogen and xylene) as illustrated in Fig. 8. It can be seen that all of the τ_{res} are less than 5 s (for methanol, τ_{res} = 3 s; isopropanol, τ_{res} = 3 s; actone, τ_{res} = 4 s; hydrogen, τ_{res} = 1 s; xylene, τ_{res} = 5 s), while the τ_{recov} are in the range of 9-15 s (for methanol, τ_{recov} = 9 s; isopropanol, τ_{recov} = 13 s; actone, τ_{recov} = 7 s; hydrogen, τ_{recov} = 15 s; xylene, τ_{recov} = 10 s). In addition, the response and recovery speeds of our sensor are among the fastest in contrast to the reported SnO_2-based gas sensors recently (Table S1, ESI†), further demonstrating the excellent response/recovery behavior of our SnO_2 NSs@SiC NFs gas sensor. Fig. 8f shows the sensing selectivity of SnO_2 NSs@SiC NFs sensor upon exposure to various gases, including ethanol, methanol, isopropanol, actone, hydrogen and xylene. Among the investigated gases, the sensor shows the strongest response toward ethanol, which is 1.6 times to hydrogen and 2~4 times to other gases. The result suggests the prepared SnO_2 NSs@SiC NFs sensor exhibits an ethanol sensing selectivity. The different adsorption abilities and activities of different target gases on the SnO_2 NSs@SiC NFs are different at a given temperature, which may be result in the superior sensing selectivity of SnO_2 NSs@SiC NFs.[18]

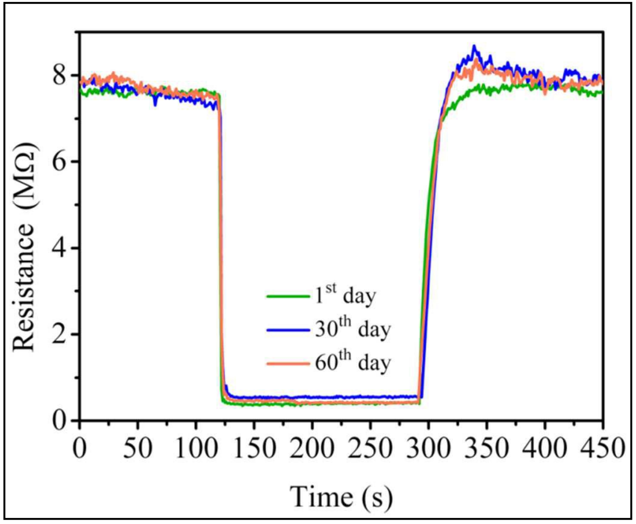

Fig. 9 The response/recovery behaviors of the hierarchical SnO_2 NSs@SiC NFs sensor after 30 and 60 days, implying the superior long-term stability of the sensor.

The sensing performances of SnO_2 NSs@SiC NFs sensor towards ethanol were measured after 30 and 60 days, respectively, to investigate the long-term stability of the sensor. As shown in Fig. 9, the gas sensor displays a constant response/recovery behavior as well as the sensitivity toward ethanol after 30 and 60 days, demonstrating the superior long-term stability of SnO_2 NSs@SiC NFs.

Collectively, the SnO_2 NSs@SiC NFs sensor shows high sensitivity, excellent reproducibility, good sensing selectivity, outstanding long-term stability and particularly ultrafast response/recovery speed toward ethanol, even at high temperature. A proposed sensing mechanism is illustrated in Fig. 10. Firstly, the ultrathin SnO_2 NSs with high surface-to-volume ratio were vertically grown on the SiC NFs, supplying a three-dimensional attacking possibility for the target gases. The target gases can react with oxygen species on the SnO_2 NSs from discretional direction. Benefiting from the hierarchical architectures, each of the SnO_2 NSs on the SiC NFs contributes to the sensing sites, while the pure SnO_2 NSs have a relatively low sensing area because of its aggregation. Secondly, thanks to in situ fabrication process as illustrated in Scheme 1, the SiC NFs and SnO_2 NSs are tightly connected to form a heterojunction. And the potential barrier between SnO_2 and SiC is very low since the work function of SnO_2 (4.5-4.9 eV)[11,42] is just a little smaller than that of SiC (4.5-5.2 eV).[43,44] These two reasons make it easy for the electron transfer from the CB of SiC to the CB of SnO_2, and simultaneously the holes on the valance band (VB) of SnO_2 can travel to the VB of SiC. At the same time, a built-in potential barrier between SiC NFs and SnO_2 NSs is established. The efficient charge separation extends the lifetime of the charge carriers, promoting the charge transfer efficiency of the interface to SnO_2.[45] Thirdly, the ultrathin SnO_2 NSs are tightly connected together forming homojunction potential barrier between SnO_2 NSs. Blocked by the built-in potential barrier and homojunction potential barrier, the electron transporting in the system is greatly restricted. Thereupon, more oxygen species are absorbed on the surface of SnO_2 NSs (in SnO_2 NSs@SiC NFs) due to the extra electrons on SnO_2 NSs, which are provided by the migration of electrons at the heterojunction interface. For reducing target gases (denoted as R, electron donor), more gas molecules can be oxidized by the oxygen species ($R + O^- \rightarrow RO + e^-$). Thus larger amounts of electrons will release back to SnO_2 NSs, further decreasing the resistance of SnO_2 NSs@SiC NFs sensor. It has also been demonstrated that the resistance is exponentially proportional to the effective barrier height, $R=R_0\exp(qV/kT)$, where R and R_0 are accordingly the real and initial resistances of the sensor, qV is the potential barrier height.[46] Obviously, the reaction between the target gases and sensor will change the two potentials barrier in the sensor system, further leading to the significant change in the resistance of the sensor. As a consequence, the SnO_2 NSs@SiC NFs sensor shows a higher response than the SnO_2 NSs sensor.

Although a relatively fast response/recovery speed can be obtained at higher temperature due to the more energy to accelerate the desorption of gases and the reaction between target gases and the sensing materials, that is not the main reason in the case of our SnO_2 NSs@SiC NFs sensor. In fact, the response/recovery speed of SnO_2 NSs@SiC NFs sensor is much faster than those of the commercial SnO_2 powders and pure SnO_2 NSs sensor at the same operating temperature. It is reported that 3C-SiC owns high electron mobility due to the enhanced oxygen concentration accumulated at the crystal defects.[47-49] Therefore, the quasi-one-dimensional SiC NFs core with high aspect ratios can supply a continuous transport pathway for the fast charge transfer.[27,50] Moreover, the accessible electron transfer between the SnO_2 NSs (contacted

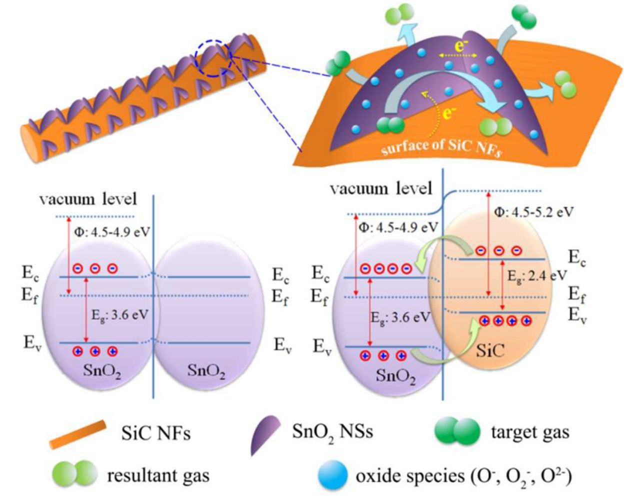

Fig. 10 Proposed sensing mechanism for the high sensitivity and ultrafast response/recovery rate of the SnO_2 NSs@SiC NFs.

closely with each other as shown in Fig. 1c) and the heterojunction of SnO_2-SiC accelerate the electron transport in the sensor. These lead to the faster response rate of the SnO_2 NSs@SiC NFs sensor. In the case of desorption process, the resultant gases can leave the surface of SnO_2 NSs@SiC NFs almost without any hindrance due to the hierarchical structure of vertical SnO_2 NSs on SiC NFs. It has been demonstrated that the hierarchical architectures can provide a way to maximize the interfacial area for effective electron transfer and gas diffusion, thus leading to fast sensing response and recovery of sensors.[51,52] However, the gases are detained by the aggregated SnO_2 of pure SnO_2 NSs sensor, which results in its slower recovery rate. Taken together, the higher response and the fast response/recovery rate of SnO_2 NSs@SiC NFs sensor are attributed to the accessible electron transfer at the interface of the SnO_2-SiC heterojuction as well as the specific hierarchical architectures of vertical ultrathin SnO_2 NSs@SiC NFs.

Conclusions

In conclusion, vertically ultrathin SnO_2 NSs were in situ gown on the quasi-one-dimensional SiC NFs forming a hierarchical architecture via a simple hydrothermal method. Compared with commercial SnO_2 powders and pure SnO_2 NSs, the SnO_2 NSs@SiC NFs hierarchical composite exhibited a superior gas sensing performance including high sensitivity, excellent reproducibility, outstanding sensing selectivity, long-term stability and particularly ultrafast response/recovery rate toward ethanol among the target gases (ethanol, methanol, isopropanol, actone, hydrogen and xylene), even at high temperature (500 °C). Such a superior sensing performance is attributed to the synergic effect of SnO_2-SiC heterojuction, the hierarchical structure as well as the vertical growth of ultrathin nanosheet morphology. This work may be directional to design high performance gas sensors for application in harsh environments.

Acknowledgments

The work was financially supported by National Natural Science Foundation of China (51173202, 51203182), Hunan Provincial Natural Science Foundation of China (13JJ4009), State Key Laboratory of Advanced Technology for Materials Synthesis and Processing (Wuhan University of Technology) (2014-KF-10), the State Key Laboratory of Refractories and Metallurgy, Wuhan University of Science and Technology (G201501) and Research Project of National University of Defense Technology (JC13-01-05). This work was also supported by Aid program for Science and Technology Innovative Research Team in Higher Educational Institutions of Hunan Province and Aid Program for Innovative Group of National University of Defense Technology.

Notes and references

1 A. Kaushik, R. Kumar, S. K. Arya, M. Nair, B. D. Malhotra and S. Bhansali, *Chem. Rev.*, 2015, **115**, 4571-4606.
2 M. W. G. Hoffmann, L. Mayrhofer, O. Casals, L. Caccamo, F. Hernandez-Ramirez, G. Lilienkamp, W. Daum, M. Moseler, A. Waag, H. Shen and J. D. Prades, *Adv. Mater.*, 2014, **26**, 8017-8022.
3 S. M. Majhi, P. Rai and Y. T. Yu, *ACS Appl. Mater. Interfaces*, 2015, **7**, 9462-9468.
4 S. Singkammo, A. Wisitsoraat, C. Sriprachuabwong, A. Tuantranont, S. Phanichphant and C. Liewhiran, *ACS Appl. Mater. Interfaces*, 2015, **7**, 3077-3092.
5 A. Das, V. Bonu, A. K. Prasad, D. Panda, S. Dhara and A. K. Tyagi, *J. Mater. Chem. C*, 2014, **2**,164-171.
6 J. H. Lee, A. Katoch, S. W. Choi, J. H. Kim, H. W. Kim, and S. S. Kim, *ACS Appl. Mater. Interfaces*, 2015, **7**, 3101-3109.
7 Z. Zhang, X. Zou, L. Xu, L. Liao, W. Liu, J. Ho, X. Xiao, C. Jiang and J. Li, *Nanoscale*, 2015, **7**, 10078-10084.
8 G. Lu, L. E. Ocola and J. Chen, *Adv. Mater.*, 2009, **21**, 2487-2491.
9 S. Xu, Y. Yang, H. Y. Wu, C. Jiang, L. Q. Jing and K. Y. Shi, *J. Inorg. Mater.*, 2013, **28**, 584-588.
10 S. H. Jeong, S. Kim, J. Cha, M. S. Son, S. H. Park, H. Y. Kim, M. H. Cho, M. H. Whangbo, K. H. Yoo and S. J. Kim, *Nano Lett.*, 2013, **13**, 5938-5943.
11 L. Xu, R. Xing, J. Song and H. Song, *J. Mater. Chem. C*, 2013, **1**, 2174-2182.
12 S. Cui, Z. Wen, X. Huang, J. Chang and J. Chen. *Small*, 2015, **11**, 2305-2313.
13 H. Wang, K. Dou, W. Y. Teoh, Y. Zhan, T. F. Hung, F. Zhang, J. Xu, R. Zhang and A. L. Rogach, *Adv. Funct. Mater.*, 2013, **23**, 4847-4853.
14 X. Chen, Z. Guo, W. H. Xu, H. B. Yao, M. Q. Li, J. H. Liu, X. J. Huang, S. H. Yu, *Adv. Funct. Mater.*, 2011, 21, 2049-2056.
15 H. R. Kim, A. H. I. D. Kim, N. Barsan, U. Weimar and J. H. Lee, *Adv. Funct. Mater.*, 2011, **21**, 4456-4463.
16 J. S. Lee, O. S. Kwon, S. J. Park, E. Y. Park, S. A. You, H. Yoon, J. Jang, *ACS Nano*, 2011, **5**, 7992-8001.
17 J. Zhang, S. Wang, M. Xu, Y. Wang, H. Xia, S. Zhang, X. Guo and S. Wu, *J. Phys. Chem. C*, 2009, **113**, 1662-1665.
18 L. Li, S. He, M. Liu, C. Zhang and W. Chen, *Anal. Chem.*, 2015, **87**, 1638-1645.
19 H. Liu, M. Li, O. Voznyy, L. Hu, Q. Fu, D. Zhou, Z. Xia, E. H. Sargent and J. Tang, *Adv. Mater.*, 2014, **26**, 2718-2724.
20 Y. Liu, J. Parisi, X. Sun and Y. Lei, *J. Mater. Chem. A*, 2014, **2**, 9919-9943.
21 M. T. Soo, K. Y. Cheong and A. F. M. Noor, *Sens. Actuators, B*, 2010, **151**, 39-55.
22 P. Tsiakarasa, A. Demin, *J. Power Sources*, 2001, **102**, 210-217.
23 S. D. Nobrega, M. V. Galesco, K. Giron, D. Z. de Florio, M. C. Steil, S. Georges, F. C. Fonseca, *J. Power Sources*, 2012, **213**, 156-159.
24 L. Li, M. Liu, S. He, W. Chen, *Anal. Chem.*, 2014, **86**, 7996-8002.
25 B. Wang, Y. Wang, Y. Lei, N. Wu, Y. Gou, C. Han, D. Fang, *J. Mater. Chem. A*, 2014, **2**, 20873-20881.
26 J. Chen, J. Zhang, M. Wang and Y. Li, *Sens. Actuators, B*, 2014, **201**, 402-406.
27 M. Kim, I. Oh and J. Kim, *J. Power Sources*, 2015, **282**, 277-285.
28 A. Karakuscu, A. Ponzoni, E. Comini, G. Sberveglieri and C. Vakifahmetoglu, *Int. J. Appl. Ceram. Technol.*, 2014, **11**, 851-857.
29 S. Ding, J. S. Chen and X. W. (David). Lou, *Adv. Funct. Mater.*, 2011, **21**, 4120-4125.
30 S. W. Choi, A. Katoch, G. J. Sun, P. Wu and S. S. Kim, *J. Mater. Chem. C*, 2013, **1**, 2834-2841.
31 Y. Bing, Y. Zeng, C. Liu, L. Qiao, B. Zou and W. Zheng, *Nanoscale*, 2015, **7**, 3276-3284.
32 C. Wang, G. Du, K. Ståhl, H. Huang, Y. Zhong and J. Z. Jiang, *J. Phys. Chem. C*, 2012, **116**, 4000-4011.
33 W. Li, S. Ma, Y. Li, G. Yang, Y. Mao, J. Luo, D. Gengzang, X. Xu and S. Yan, *Sens. Actuators, B.* 2015, **211**, 392-402.
34 C. Dong, X. Liu, X. Xiao, G. Chen, Y. Wang, I. Djerdj, *J. Mater. Chem. A*, 2014, **2**, 20089-20095.
35 W. Ke, G. Fang, Q. Liu, L. Xiong, P. Qin, H. Tao, J. Wang, H. Lei, B. Li, J. Wan, G. Yang and Y. Yan, *J. Am. Chem. Soc.*, 2015, **137**, 6730-6733.

36 Y. Wang, B. Wang, Y. Lei, N. Wu, C. Han, Y. Gou and D. Fang, *Appl. Surf. Sci.*, 2015, **335**, 208-212.
37 K. S. W. Sing, D. H. Everett, R. A. W. Haul, L. Moscou, R. A. Pierotti, J. Rouquerol and T. Siemieniewska, *Pure Appl. Chem.*, 1985, **57**, 603-619.
38 B. Mondal, B. Basumatari, J. Das, C. Roychaudhury, H. Saha, N. Mukherjee, *Sens. Actuators, B*, 2014, **194**, 389-396.
39 Y. Wang, Y. Wang, J. Cao, F. Kong, H. Xia, J. Zhang, B. Zhu, S. Wang and S. Wu, *Sens. Actuators, B*, 2008, **131**, 183-189.
40 Y. Chen, X. Wang, C. Shi, L. Li, H. Qin and J. Hu, *Sens. Actuators, B*, 2015, **220**, 279-287.
41 Q. Zhao, D. Ju, X. Deng, J. Huang, B. Cao and X. Xu, *Sci. Rep.*, 2015, **5**, 7874.
42 M. Punginsang, A. Wisitsoraat, A. Tuantranont, S. Phanichphant and C. Liewhiran, *Sens. Actuators, B*, 2015, **210**, 589-601.
43 X. Zhang, Y. Chen, W. Liu, W. Xue, J. Li and Z. Xie, *J. Mater. Chem. C*, 2013, **1**, 6479-6486.
44 Y. Yang, G. Meng, X. Liu, L. Zhang, Z. Hu, C. He and Y. Hu, *J. Phys, Chem. C Lett.*, 2008, **112**, 20126-20130.
45 G. Lu, J. Xu, J. Sun, Y. Yu, Y. Zhang and F. Liu, *Sens. Actuators, B*, 2012, **162**, 82-88.
46 J. Liu, S.Gong Q. Fu, Y. Wang, L. Quan and Z. Deng, *Sens. Actuators, B*, 2010, **150**, 330-338.
47 N. Yang, H. Zhuang, R. Hoffmann, W. Smirnov, J. Hees, X. Jiang and C. E. Nebel, *Anal. Chem.*, 2011, **83**, 5827-5830.
48 K. Rogdakis, M. Bescond, E. Bano and K. Zekentes, *Nanotechnology*, 2007, **18**, 475715.
49 M. Kim, I. Oh and J. Kim, *J. Mater. Chem. A*, 2015, **3**, 3944-3951.
50 C. Han, Y. Wang, Y. Lei, B. Wang, N. Wu, Q. Shi and Q. Li, *Nano Res.*, 2015, **8**, 1199-1209.
51 D. R. Miller, S. A. Akbar and P. A. Morris, *Sens. Actuators, B*, 2014, **204**, 250-272.
52 S. Park, H. Ko, S. Kim and C. Lee, *ACS Appl. Mater. Interfaces*, 2014, **6**, 9595-9600.

Graphical Abstract

The SnO_2 NSs@SiC NFs sensor shows an ultrafast response/recovery rate, high sensitivity, excellent reproducibility, good sensing selectivity and outstanding long-term stability toward ethanol, even at high temperature.